Ordering of the Antiferromagnetic Heisenberg Model on a Pyrochlore Slab

Takuya Arimori and Hikaru Kawamura

Department of Earth and Space Science, Graduate School of Science, Osaka University, Toyonaka 560-0043

Ordering of the geometrically frustrated two-dimensional Heisenberg antiferromagnet on a pyrochlore slab is studied by Monte Carlo simulations. The model is expected to serve as a reference system of SrCrGaO compound studied extensively. In sharp contrast to the kagomé Heisenberg antiferromagnet, the model exhibits locally non-coplanar spin structures at low temperatures, bearing nontrivial chiral degrees of freedom. We find that under certain conditions the model exhibits a novel Kosterlitz-Thouless-type transition at a finite temperature associated with these chiral degrees of freedom. Implications to experiments are discussed.

§1. Introduction

Magnetic ordering of geometrically frustrated antiferromagnets (AFs) has attracted continual interest of researchers in magnetism.[1] In geometrically frustrated AFs, spins usually sit on lattices made up of triangles or tetrahedra as elementary units, and interact antiferromagnetically with their neighboring spins. Intrinsic inability to simultaneously satisfy all antiferromagnetic nearest-neighbor interactions on a triangle or on a tetrahedron necessarily leads to macroscopic frustration. This makes the spin ordering on these lattices a highly nontrivial issue. Triangles- or tetrahedra-based lattices might be classified into two categories: One is the tightly coupled lattice consisting of *edge*-sharing triangles or tetrahedra, and the other is the loosely-coupled lattice consisting of *corner*-sharing triangles or tetrahedra. Examples of the former are the triangular lattice in two dimensions (2D) and the stacked-triangular lattice in three dimensions (3D), while those of the latter are the 2D kagomé lattice and the 3D pyrochlore lattice. In earlier studies, emphasis was put on the former category.[2,3] These studies revealed a variety of interesting ordering phenomena not encountered in standard unfrustrated magnets, *e.g.*, novel universality classes, exotic phase transition such as chiral transition and new type of topological phase transition *etc*.

Recently, interest has been focused more on the latter category, *i.e.*, the 2D kagomé and 3D pyrochlore AFs.[4–6] Due to the looser coupling among the frustrating units, these systems often remain paramagnetic down to very low temperatures without any magnetic ordering. Indeed, various theoretical studies on the 2D kagomé and 3D pyrochlore AFs have revealed that these systems

remain paramagnetic down to zero temperature without any phase transition.[7–10] Experimentally, however, many of the geometrically frustrated magnets, which are regarded as typical kagomé or pyrochlore AFs, exhibit a phase transition at a low but finite temperature, quite often a spin-glass (SG)-like freezing transition.[4–6]

One of the best studied geometrically frustrated AFs is the $S = 3/2$ Heisenberg kagomé AF SrCrGaO (SCGO).[4,5] Experimentally, this material exhibits a SG-like transition at a finite temperature $T = T_f$ as in many other geometrically frustrated AFs, although T_f is considerably lower than the Curie-Weiss temperature of this material due to the strong geometrical frustration.[11,12] In spite of extensive experimental and theoretical efforts, the true nature of this SG-like transition of SCGO has remained elusive. Extensive Monte Carlo (MC) simulations performed for the 2D kagomé Heisenberg AF have failed to reproduce the SG-like transition as experimentally observed in SCGO, suggesting that the modeling of SCGO as a pure kagomé AF might be inadequate in capturing some essential aspects of this material.

Although SCGO has been regarded for some time as a typical model compound of the 2D kagomé AF, the underlying lattice structure is in fact not of a pure (single-layer) kagomé lattice, but rather, of a kagomé sandwich, or a "pyrochlore slab".[4,5,11,12] The structure of the lattice is illustrated in Fig.1(a): It consists of two 2D kagomé layers which sandwiches the sparse triangular layer in between. Note that this lattice is obtained by slicing the 3D pyrochlore lattice along the (111) direction into the slab geometry. Inelastic neutron-scattering measurements have indicated that the neighboring slabs are magnetically well separated along the c-axis.[13] Hence, in modeling SCGO, one may safely neglect the inter-slab interaction and consider the 2D Heisenberg model on a pyrochlore-slab lattice.

The purpose of the present paper is to study the ordering properties of the antiferromagnetic classical Heisenberg model on the pyrochlore-slab lattice by means of MC simulations, and to examine whether some new features which are different from those of the well-studied pure kagomé Heisenberg AF would arise, possibly due to the tetrahedron-based structure of this lattice. In particular, we pay attention to the possible "chiral" properties of the model. "Chirality" is a multi-spin quantity representing the sense or handedness of the local non-coplanar spin structures induced by spin frustration. It is defined for three neighboring Heisenberg spins as a pseudo-scalar, $\chi = \boldsymbol{S}_1 \cdot \boldsymbol{S}_2 \times \boldsymbol{S}_3$, so as to give a nonzero value if the the three spins make non-coplanar configurations but vanish otherwise. This type of chirality is sometimes called "scalar chirality", which is distinct from the "vector chirality" often used in the literature, defined for two neighboring Heisenberg spins by an axial vector $\boldsymbol{S}_1 \times \boldsymbol{S}_2$.[14] In the case of the pure kagomé Heisenberg AF, it has been known that the spin structure selected at low temperatures is a coplanar one with the vanishing scalar chirality.[7,9] In sharp contrast, we shall show below that in the case of the pyrochlore-slab Heisenberg AF the spin structure stabilized at low temperatures is a *non-coplanar* one sustaining

nontrivial chiral degrees of freedom. Depending on the parameter values of our model Hamiltonian, these nontrivial chiral degrees of freedom are found to exhibit novel thermodynamic phase transition at a finite temperature without accompanying the order of Heisenberg spins. Such chiral phase transition, unexpected so far, does not occur in the kagomé Heisenberg AF.

In section 2, we introduce our model and explain some of the details of our numerical method. Our model Hamiltonian possesses, within the kagomé layers, the antiferromagnetic nearest-neighbor (nn) coupling $J_1 > 0$ and next-nearest-neighbor (nnn) coupling J_2 of either sign, while it possesses, between the kagomé layers and the triangular layer, the antiferromagnetic nn coupling $J' > 0$. Various physical quantities calculated in MC simulations are defined in section 3. The results of our MC simulations are presented in section 4. The cases of vanishing, antiferromagnetic and ferromagnetic nnn interactions, $i.e.$, the cases of $J_2 = 0$, $J_2 > 0$, $J_2 < 0$, are dealt with in section 4.1, 4.2 and 4.3, respectively. In all cases studied, the system is found to sustain nonzero local chiralities, in sharp contrast to the pure kagomé Heisenberg AF. Furthermore, in the particular case of the antiferromagnetic nnn coupling $J_2 > 0$, we find that the model exhibits a Kosterlitz-Thouless-type transition associated with the chiralities. Section 5 is devoted to summary and discussion. Implication to experiments is briefly discussed.

§2.   The Model and the Method

The model we consider is the isotropic classical Heisenberg model on a pyrochlore-slab (or kagomé-sandwich) lattice. The pyrochlore-slab lattice is illustrated in Fig.1(a). It consists of two 2D kagomé layers of lattice spacing d which sandwiches the sparse triangular layer of lattice spacing $2d$ in between. The unit cell of the lattice may be taken as two corner-sharing tetrahedra containing seven sites numbered from 1 to 7, which is illustrated by the solid lines in Fig.1(a). Among these seven sites belonging to a unit cell, the lower threes forming the equilateral triangle (the sites 1, 2 and 3 in Fig.1(a)) are parts of the lower kagomé layer, the upper threes forming the equilateral triangle (the sites 5, 6 and 7) are parts of the upper kagomé layer, and the one in the middle (the site 4) is a part of the sparse triangular layer. These unit cells containing seven sites are arranged forming the 2D triangular lattice of spacing $2d$. In Fig.1(b), we show the lower kagomé layer, which consists of only the sites 1, 2 and 3. Note that the upward triangle in Fig.1(b) corresponds to the bottom plane of tetrahedron with an apical site 4 on top of it, while the downward triangle is not a part of any tetrahedron. These upward triangles are further grouped into three types, denoted A, B and C, each forming triangular sublattices of spacing $2\sqrt{3}d$ (recall here that the triangular lattice can be decomposed into three inter-penetrating triangular sublattices). We shall use such representation of the lattice later.

Our Hamiltonian is given by

$$\mathcal{H} = J_1 \sum_{\langle ij \rangle}^{n.n.} \boldsymbol{S}_i \cdot \boldsymbol{S}_j + J_2 \sum_{\langle kl \rangle}^{n.n.n.} \boldsymbol{S}_k \cdot \boldsymbol{S}_l + J' \sum_{\langle mn \rangle} \boldsymbol{S}_m \cdot \boldsymbol{S}_n, \tag{1}$$

where $J_1 > 0$ is the antiferromagnetic nn interaction on the two kagomé layers, J_2 is the nnn interaction on the kagomé layers, and $J'(>0)$ is the antiferromagnetic nn interaction between the kagomé layers and the triangular layer: See Fig.1(a). The first and second sums in eq.(1) are taken over all nn and nnn pairs on the two kagomé layers, while the third sum is taken over all nn pairs linking the triangular layer and the two kagomé layers. The variable $\boldsymbol{S}_i$ is a three-component unit vector representing a classical Heisenberg spin at the i-th site.

In order to investigate the thermodynamic properties of this model, we perform the standard heat-bath MC simulations. Since the present model is a highly frustrated model possessing many degenerate states, possibly leading to very slow relaxation, we combine the heat-bath method with the temperature-exchange technique to facilitate efficient thermalization.[15] Simulations are made for a pyrochlore-slab lattice with $N = 7 \times L \times L$ spins with $L =$6, 12, 18, 24 and 30, where the number seven here represents the number of spins per unit cell. Periodic boundary conditions are employed.

Typically, initial 2×10^6 Monte Carlo steps per spin (MCS) are discarded for thermalization, and the following 1.8×10^7 MCS are used to calculate various physical quantities. The latter 1.8×10^7 MCS is divided into 5 bins, and the error bars are estimated from the standard deviation of the data sets taken for these 5 bins.

Although our model is a regular one without any quenched randomness, it turns out to be a hard-relaxing system due to its severe frustration, exhibiting very slow relaxation at low temperatures similar to the ones encountered in spin glasses. Therefore, we pay special attention to be sure that the system is fully thermalized. Equilibration is checked by the following procedures: First, we monitor the system to travel back and forth many times during the the temperature-exchange process (typically more than 10 times) between the maximum and minimum temperature points, and check at the same time that the relaxation due to the standard heat-bath updating is reasonably fast at the highest temperature, whose relaxation time is of order 10^2 MCS. This guarantees that significantly different parts of the phase space is sampled in each "cycle" of the temperature-exchange process. Second, we monitor the stability of the calculated physical quantities to check that they remain stable during at least three times longer MC period.

§3.   Physical Quantities

In this section, we define various physical quantities calculated in our simulations below. Energy, specific heat and uniform magnetic susceptibility are defined and calculated in the standard

way. We calculate in addition the nonlinear magnetic susceptibility χ_2, according to the relation,

$$\chi_2 = \frac{1}{6Nk_{\mathrm{B}}T}(\langle M_z^4 \rangle - 4\langle M_z \rangle \langle M_z^3 \rangle - 3\langle M_z^2 \rangle^2 + 12\langle M_z^2 \rangle \langle M_z \rangle^2 - 6\langle M_z \rangle^4), \tag{2}$$

where M_z is the z-component of the total magnetization of the system, and $\langle \cdots \rangle$ represents the thermal average. One generally expects that there should be no long-range order (LRO) of Heisenberg spin, nor a finite-temperature transition occurring in its spin sector, in a fully isotropic Heisenberg model in two spatial dimensions like our model. Nevertheless, in order to probe the possible development of the spin short-range order (SRO), we follow the previous works on the pure kagomé AF and calculate the following two Fourier modes of spin order, the $q = 0$ mode and the $\sqrt{3} \times \sqrt{3}$ mode, each being the representative ordering mode of the kagomé lattice.[7,9] The Fourier magnetization associated with the $q = 0$ mode is defined by

$$m_0 = \langle |\boldsymbol{m}_0|^2 \rangle^{1/2}, \tag{3}$$

$$\boldsymbol{m}_0 = \frac{\sqrt{2}}{3N_s} \sum_{i,\alpha} \boldsymbol{S}_i^\alpha \exp(\mathrm{i}\phi_\alpha), \tag{4}$$

where $N_s = L \times L$ denotes the total number of unit cells, and $(\phi_1, \phi_2, \phi_3) = (0, 2\pi/3, 4\pi/3)$. The summation over i is taken over N_s unit cells and that over $1 \leq \alpha \leq 3$ is taken over three sites in a unit cell lying on the lower kagomé layer. Note that m_0 gives unity when the spin configuration is in the $q = 0$ state. The Fourier magnetization associated with the $\sqrt{3} \times \sqrt{3}$ mode is defined by

$$m_{\sqrt{3}} = \langle |\boldsymbol{m}_{\sqrt{3}}|^2 \rangle^{1/2}, \tag{5}$$

$$\boldsymbol{m}_{\sqrt{3}} = \frac{\sqrt{2}}{3N_s}(\sum_{i\in A,\alpha} \boldsymbol{S}_i^\alpha \exp(\mathrm{i}\phi_\alpha^A) + \sum_{i\in B,\alpha} \boldsymbol{S}_i^\alpha \exp(\mathrm{i}\phi_\alpha^B) + \sum_{i\in C,\alpha} \boldsymbol{S}_i^\alpha \exp(\mathrm{i}\phi_\alpha^C)), \tag{6}$$

where $(\phi_1^A, \phi_2^A, \phi_3^A) = (0, 2\pi/3, 4\pi/3)$, $(\phi_1^B, \phi_2^B, \phi_3^B) = (2\pi/3, 4\pi/3, 0)$, $(\phi_1^C, \phi_2^C, \phi_3^C) = (4\pi/3, 0, 2\pi/3)$, while A, B and C denote the three triangular sublattices shown in Fig.1(b). Note that $m_{\sqrt{3}}$ gives unity when the spin configuration is in the $\sqrt{3} \times \sqrt{3}$ state. In our definition of $\boldsymbol{m}_{\sqrt{3}}$ and $\boldsymbol{m}_0$ above, we have implicitly assumed that the antiferromagnetic J_1 tends to align any three spins at each elementary triangle into the $120°$ spin structure in which neighboring spins make an angle equal to $2\pi/3$ with each other.

One can also define the Binder ratio associated with these ferrimagnetic order parameters. For example, the Binder ratio associated with the $q = 0$ mode may be defined by

$$g_0 = 4 - 3\frac{\langle |\boldsymbol{m}_0|^4 \rangle}{\langle |\boldsymbol{m}_0|^2 \rangle^2}. \tag{7}$$

Here, g_0 is defined so that in the thermodynamic limit it vanishes in the high-temperature phase while it gives unity in the non-degenerate ordered phase. We have used the fact that the order parameter considered here has six independent components.

As mentioned, we are particularly interested in the ordering behavior of the chirality. Generally, the local chirality may be defined for three neighboring Heisenberg spins. Here, we calculate the local chirality for the three spins located at each upward triangle on the lower kagomé layer (the spins 1, 2, 3 in Fig.1(b)),

$$\chi_i = \boldsymbol{S}_i^1 \cdot (\boldsymbol{S}_i^2 \times \boldsymbol{S}_i^3). \tag{8}$$

The upward triangle on the lower kagomé layer corresponds to the bottom plane of tetrahedron. Chirality may also be defined for other types of triangles as well. We supplementarily calculate the local chirality defined for three Heisenberg spins on the downward triangle on the lower kagomé layer which is not a part of any tetrahedron,

$$\chi_i^{\text{tri}} = \boldsymbol{S}_i^1 \cdot (\boldsymbol{S}_j^2 \times \boldsymbol{S}_k^3). \tag{9}$$

In order to measure the local non-coplanarity of the spin structure, we compute the mean local amplitude of these chiralities,

$$\bar{\chi}^2 = \frac{1}{N_s} \sum_i \langle \chi_i^2 \rangle, \quad \bar{\chi}_{\text{tri}}^2 = \frac{1}{N_s} \sum_i \langle (\chi_i^{\text{tri}})^2 \rangle. \tag{10}$$

These quantities vanish for coplanar spin structures, and its magnitude tells us the extent of the non-coplanarity of the local spin structures. Previous studies have revealed that these quantities tend to vanish at low temperatures in the pure kagomé Heisenberg AF.[7,9]

In order to detect the ordering of the chirality, we calculate the ferrimagnetic (or staggered) chiral order parameter, $m_{\chi f}$, defined by

$$m_{\chi f}^2 = (m_\chi^A)^2 + (m_\chi^B)^2 + (m_\chi^C)^2 - m_\chi^A m_\chi^B - m_\chi^B m_\chi^C - m_\chi^C m_\chi^A, \tag{11}$$

$$m_\chi^A = \frac{3}{N_s} \sum_{i \in A} \chi_i, \quad m_\chi^B = \frac{3}{N_s} \sum_{i \in B} \chi_i, \quad m_\chi^C = \frac{3}{N_s} \sum_{i \in C} \chi_i. \tag{12}$$

This quantity gives a nonzero value if the chirality exhibits a ferrimagnetic order with $\sqrt{3} \times \sqrt{3}$ periodicity, characterized by the wavevectors $\pm\boldsymbol{Q} = (\pm 4\pi/3d', 0)$, where $d' = 2d$ is the lattice constant of the triangular lattice.

The associated chiral Binder ratio may be defined by

$$g_{\chi f} = 2 - \frac{\langle m_{\chi f}^4 \rangle}{\langle m_{\chi f}^2 \rangle^2}. \tag{13}$$

Note that $g_{\chi f}$ is defined here so that in the thermodynamic limit it vanishes in the high-temperature phase while it gives unity in the non-degenerate ordered phase.

Further information on the ferrimagnetic chiral order can be obtained via the "phase variable" θ, defined as follows. By introducing the "real" (or cosine) and the "imaginary" (or sine) parts of the Fourier magnetization by

$$m_\chi^R = \frac{1}{2}(2m_\chi^A - m_\chi^B - m_\chi^C), \tag{14}$$

$$m_\chi^I = \frac{\sqrt{3}}{2}(m_\chi^C - m_\chi^B), \tag{15}$$

we define the phase θ by

$$\theta = \arg(m_\chi^R + \mathrm{i}m_\chi^I). \tag{16}$$

If the ordered state is in the "cosine" state with, say, $m_\chi^A : m_\chi^B : m_\chi^C = 1 : 1 : -1$, then the phase θ becomes a multiple of $\pi/3$, *i.e.*, it is equal to $\frac{\pi}{3}n$, with n being an integer. On the other hand, if the ordered state is in the "sine state" (or in the so-called partial disordered state) with, say, $m_\chi^A : m_\chi^B : m_\chi^C = 1 : 0 : -1$, then the phase θ is equal to $\frac{\pi}{3}(n + \frac{1}{2})$.

So far, we have dealt with the possible ferrimagnetic $\sqrt{3} \times \sqrt{3}$ ordering of the chirality. In a highly frustrated model like our model, chiralities might possibly be ordered into more complicated spatial patterns, or even into spatially random patterns without any spatial periodicity. In order not to miss such possibilities, we also calculate the Edwards-Anderson-type chiral order parameter used in the study of spin glasses, "chiral-glass order parameter".[16] For this, we first introduce the replica overlap of the scalar chirality q_χ, by considering two independent systems ("replicas") described by the same Hamiltonian (1), via the relation,

$$q_\chi = \frac{1}{N_\mathrm{s}} \sum_i \chi_i^{(1)} \chi_i^{(2)}, \tag{17}$$

where $\chi_i^{(1)}$ and $\chi_i^{(2)}$ represent the chiral variables defined at the i-th upward triangle on the lower kagomé layer of the replicas 1 and 2, respectively. In our simulations, we prepare the two replicas 1 and 2 by running two independent sequences of systems in parallel with different spin initial conditions and different sequences of random numbers. In terms of this chiral overlap q_χ, the chiral-glass order parameter may be defined by

$$q_\chi^{(2)} = \langle q_\chi^2 \rangle \ . \tag{18}$$

This quantity gives a nonzero value if there occurs any type of chirality ordering, either being periodic or random.

§4.   Monte Carlo Results

In this section, we present the results of our MC simulations. This section is divided into three subsections. In §4.1, we first deal with the case of vanishing nnn interaction in the kagomé layers, *i.e.*, the case $J_2 = 0$. The cases of the antiferromagnetic and ferromagnetic nnn interaction in the kagomé layers, $J_2 > 0$ and $J_2 < 0$, are dealt with subsequently in §4.2 and §4.3.

4.1   The case of vanishing next-nearest-neighbor interaction: $J_2 = 0$

First, we consider the case in which the interaction in the kagomé layers works only between nearest neighbors, *i.e.*, the case $J_2 = 0$. In Fig.2, we show the temperature and size dependence of the specific heat per spin. The specific heat gradually increases with decreasing temperature, without showing any prominent feature. In the low-temperature limit $T \to 0$, the specific heat tends to the asymptotic value, $C(T \to 0) \simeq 0.845$, which is considerably smaller than the spin-wave value, unity, expected in the standard classical Heisenberg model. Similar deviation from the spin-wave value has been known to occur in the pure kagomé Heisenberg AF,[7,9,10] and is a manifestation of the severe frustration of the model.

In Fig.3, we show the temperature and size dependence of the linear and nonlinear susceptibilities per spin. No anomalous behavior is appreciable in these quantities. The linear susceptibility exhibits only weak temperature dependence, while the nonlinear susceptibility stays zero within the error bars.

In Fig.4, we show the the temperature and size dependence of the ferrimagnetic magnetizations associated with the $q = 0$ and the $\sqrt{3} \times \sqrt{3}$ modes, m_0 and $m_{\sqrt{3}}$. One can see from the figures that both m_0 and $m_{\sqrt{3}}$ stay small even at lower temperatures, and that there is no appreciable selection between these two modes. This is in contrast to the behavior of the pure kagomé Heisenberg AF where the $\sqrt{3} \times \sqrt{3}$ mode is selected over the $q = 0$ mode at low temperatures.[7,9] Thus, the development of even the spin SRO is largely suppressed in the present model.

The results of the chirality-related quantities are given in Figs.5 and 6. In Fig.5, we show the temperature and size dependence of the mean local amplitude of the chiralities. As can clearly be seen from the figure, $\bar{\chi}$ has a nonzero value even in the $T \to 0$ limit, while $\bar{\chi}_{\mathrm{tri}}$ tends to zero. This observation indicates that the spins on tetrahedron form locally non-coplanar structures, while the spins not belonging to tetrahedron form locally coplanar structures. In any case, the fact that the spins on tetrahedron form the non-coplanar structures at low temperatures sustaining the nontrivial chirality forms the basis of our following analysis.

Once establishing the existence of nontrivial local chirality, the next obvious question is how these chiralities order with decreasing temperature. In Fig.6, we show the size and temperature dependence of the chiral-glass order parameter $q_\chi^{(2)}$. As is evident from the figure, $q_\chi^{(2)}$ does not grow with decreasing temperature, rapidly decreasing with increasing L. This indicates that the chirality

remains fluctuating until low temperature without a finite-temperature transition. Thus, in the case of $J_2 = 0$, although the chirality certainly becomes nontrivial locally, it remains fluctuating until low temperatures without exhibiting thermodynamic phase transition. The absence of chiral transition in the $J_2 = 0$ case is easy to understand, if one notes the fact that the *next-nearest-neighbor* interaction is necessary in order to directly couple the neighboring tetrahedra on the kagomé layers at which the chirality becomes nontrivial.

4.2   The case of antiferromagnetic next-nearest-neighbor interaction: $J_2/J_1 = 0.5$

   In this subsection, we consider the case in which the nnn interaction on the kagomé layers is antiferromagnetic, fixing its magnitude to be $J_2 = 0.5J_1$. The inter-plane interaction J' is set equal to J_1 for the time being. The other choice of J' will be considered later in this subsection.

   In Fig.7, we show the temperature and size dependence of the specific heat per spin. In contrast to the $J_2 = 0$ case, the data show double peaks, the higher one at $T = T_{p1} \simeq 0.29J_1$ and the lower one at $T = T_{p2} \simeq 0.09J_1$. Such double-peak feature in the specific heat has not been observed in the pure kagomé Heisenberg AF.[7,9)] The size dependence of these specific-heat peaks reveals that the peak heights eventually saturate with L, suggesting that both peaks are non-divergent; either a non-divergent singularity with $\alpha < 0$, or a regular peak without any singularity.

   In Fig.8, we show the temperature and size dependence of the linear and nonlinear magnetic susceptibilities per spin. While the nonlinear susceptibility exhibits no appreciable anomaly as in the case of $J_2 = 0$, the linear susceptibility exhibits a clear cusp-like anomaly at $T/J_1 \simeq 0.085$ close to the lower specific-heat peak, which has not been seen in the $J_2 = 0$ case.

   The origin of the higher specific-heat peak may be seen from Fig.9, where we show the temperature and size dependence of the ferrimagnetic magnetizations associated with the $q = 0$ and the $\sqrt{3} \times \sqrt{3}$ modes, m_0 and $m_{\sqrt{3}}$, respectively. One can see from the figures that the $q = 0$ mode is dominant over the $\sqrt{3} \times \sqrt{3}$ mode, the SRO of which begins to grow around the higher specific-heat peak temperature T_{p1}. This indicates that the higher specific-heat peak is associated with the development of the $q = 0$ SRO of Heisenberg spins. Closer inspection of Fig.9 reveals that, around the lower specific-heat peak temperature T_{p2}, m_0 tends to be suppressed with further lowering the temperature. We shall return to this point later.

   Since our model is the isotropic Heisenberg model in 2D, one generally expects that there is no spin LRO and even m_0 should vanish in the $L \to \infty$ limit at any finite temperature. In Fig.10, we show the the temperature and size dependence of the spin Binder ratio associated with the $q = 0$ mode, g_0. With increasing L, the data monotonically decreases toward zero, suggesting that there is indeed no ordering in the spin sector at any finite temperature.

   What happened around T_{p2} or the susceptibility-cusp temperature may be seen from Figs.11 and 12 where we show the chirality-related quantities. The temperature and size dependence of the mean local amplitude of the chiralities are shown in Fig.11. The data indicate that, as in the $J_2 = 0$

case, the spins belonging to tetrahedron form locally non-coplanar structures sustaining nontrivial chirality. A very interesting observation comes out from Fig.12, where we show the temperature and size dependences of the ferrimagnetic chiral order parameter $m_{\chi f}$ and of the chiral-glass order parameter $q_\chi^{(2)}$. One can see from the figures that $m_{\chi f}$ and $q_\chi^{(2)}$ grow rather sharply around the temperature close to T_{p2} or the susceptibility-cusp temperature. This suggests that the lower specific-heat peak is somehow correlated with the onset of the ferrimagnetic order of the chirality.

In Fig.13, we show the temperature and size dependences of the Binder ratio of the ferrimagnetic chiral order parameter, $g_{\chi f}$. For smaller sizes, the calculated $g_{\chi f}$ for various L tend to cross at $T = T_c \simeq 0.082J_1$ but for larger sizes they tend to merge at $T \leq T_c$, signaling the occurrence of a phase transition of the chirality. The estimated transition temperature $T_c/J_1 = 0.082(2)$ is in rough agreement with the susceptibility-cusp temperature estimated above, and is slightly below the lower specific-heat peak temperature T_{p2}. Meanwhile, there is no appreciable anomaly in the specific heat just at $T = T_c \simeq 0.082J_1$: See the inset of Fig.7. A merging behavior of the Binder ratio, without accompanying the discernible specific-heat anomaly just at T_c but only with a non-divergent peak slightly above T_c, suggests that the observed chirality transition might essentially be of the Kosterlitz-Thouless (KT)-type.[17]

In order to investigate the nature of this chiral transition at $T = T_c$ in more detail, we show in Fig.14(a) the L-dependence of the ordering susceptibility $N_s m_{\chi f}^2$ associated with the ferrimagnetic chiral order on a log-log plot for several temperatures. As can be seen from the figure, while the data at higher temperatures exhibit the characteristic behaviors of the disordered phase, bending down toward some finite values, those at $T \leq T_c \simeq 0.082J_1$ lie on straight lines, exhibiting the behavior expected for the KT-like critical phase with algebraically-decaying correlations. The estimated slope of the plots, which should be equal to $2 - \eta$ with η being the critical-point decay exponent, is shown in Fig.14(b) as a function of temperature. More precisely, we plot the quantities

$$2 - \eta(T, L, L') = \frac{\ln(m_{\chi f}^2(L)/m_{\chi f}^2(L'))}{\ln(L/L')}, \tag{19}$$

calculated for various combinations of L and L'. As can be seen from Fig.14(b), the estimated η is found to be around $1/4$ at $T = T_c \simeq 0.082J_1$, which gradually decreases (or $2 - \eta$ increases) with decreasing temperature. This again indicates that the chiral transition at $T = T_c$ is the KT-type transition.

Indeed, there is a good reason to expect such a KT-type transition for the present chiral transition. As mentioned, chirality is an Ising like quantity taking values either positive or negative at each upward triangles in the kagomé layer. Since these upward triangles form the triangular lattice in themselves, there is a close similarity between the chirality ordering of the present model and the ordering of the 2D Ising model on the triangular lattice. If the triangular Ising model possesses the antiferromagnetic nn interaction and ferromagnetic nnn interaction, the model is

known to exhibit a three-sublattice $\sqrt{3} \times \sqrt{3}$ ordering at a finite temperature via the KT-type transition characterized by the exponent $\eta = 1/4$.[18–21] Since the chirality ordering of the present model with $J_2 > 0$ is essentially the staggered one, as is evident from the observed growth of the $\sqrt{3} \times \sqrt{3}$ component in Fig.12(a), it would be no surprise that the chirality ordering here is essentially of the KT-type.

There are two possibilities concerning the $\sqrt{3} \times \sqrt{3}$ ordering pattern in the KT phase: One is the cosine phase characterized by the sublattice magnetizations of the type $(+, +, -)$ *etc.*, and the other is the sine phase (or the partial disordered phase) characterized by the sublattice magnetizations of the type $(+, 0, -)$ *etc.* In order to see which pattern is actually realized in the present model, we show in Fig.15 the calculated two-dimensional distribution of (m_χ^R, m_χ^I), at a temperature $T/J_1 = 0.044$ well below $T_c/J_1 \simeq 0.082$. Fig.15 shows that the system predominantly stays at the phase θ being equal to $\frac{\pi}{3}(n + \frac{1}{2})$, indicating that the sine or the partial disordered state of chirality is realized. In other words, the chirality is ordered into the $(+, 0, -)$ pattern, keeping one of three sublattices totally disordered. The sixfold symmetry of the data shown in Fig.15 is a manifestation of the sixfold degeneracy of the ordered state. In fact, the antiferromagnetic ordering pattern of the Ising-like variables on three triangular sublattices can be mapped onto the ordering pattern of the 2D ferromagnetic six-clock model,[22] which is also known to exhibit the KT transition at a finite temperature with the exponent $\eta = 1/4$.[23]

It should be noticed that the triangular Ising AF with the ferromagnetic nnn interaction exhibits another phase transition with decreasing temperature, into the low-temperature phase with a finite LRO.[18–21] The exponent η at this second phase transition point is believed to be $1/9$.[21, 23] Therefore, we search for this second phase transition into the long-range-ordered state in our present model. From Fig.14(b), one sees that, even in the low-temperature regime where the estimated η comes down to $1/9$, there is no sign that the system exhibits the second transition into the long-range-ordered state where η should vanish. In other quantities such as the specific heat or the susceptibility, we do not find any evidence of the second phase transition. Presumably, severe frustration inherent to the present model might hinder the onset of the true chiral LRO. However, since our low-temperature data are limited due to the difficulty of thermalization, we cannot completely exclude the possible occurrence of such a second phase transition in our model.

In fact, the value of $m_{\chi f}$, extrapolated to $T = 0$ in Fig.12(a) and normalized by $\bar{\chi}(T \to 0)$, is only 12% of the value expected if the chirality is fully ordered into the sine pattern. Likewise, the value of $q_\chi^{(2)}$, extrapolated to $T = 0$ in Fig.12(b) and normalized by the appropriate powers of $\bar{\chi}(T \to 0)$, is only 20% of the value expected if the chirality is fully frozen over the system. These observations indicate that, even in the ordered state, chiralities are still strongly fluctuating, only a fraction of them taking part in the chirality ordering.

We also mention here that the decrease of the $q = 0$ Fourier magnetization below T_c observed

in Fig.9(a) could be understood if one notes the fact that the perfect $q = 0$ spin order tends to compete with the local non-coplanarity of spins. In fact, the antiferromagnetic nn interaction J_1 prefers the planar $120°$ spin structure at each downward triangle, which induces the planar state for the $q = 0$ spin state. Hence, the onset of the KT order of the chirality below T_c necessarily compete with the $q = 0$ spin order, and suppresses it. Such suppression of the $q = 0$ spin order below T_c can also be seen in the behavior of the chiral Binder ratio in Fig.10.

So far, we have considered the case where the inter-plane interaction J' is equal to the intra-plane nn interaction J_1. In real experimental systems, however, such equality is not expected in general. Therefore, in order to examine the possible effect of varying the inter-plane coupling, we deal with the case $J' = 0.5J_1$ (and $J_2 = 0.5J_1$ as before) in the remaining part of this subsection.

We find that most of the calculated physical quantities behave similarly to those in the $J' = J_1$ case shown above. As an example, we show in Figs.16-18 the temperature and size dependences of the specific heat, the linear susceptibility, and the chiral Binder ratio. These data indicate that the system exhibits a chiral KT transition at $T_c/J_1 = 0.029(3)$. The exponent η at $T = T_c$ is again consistent with the KT value $\eta = 1/4$ as can be seen from Fig.19. We find no evidence of the occurrence of the second transition into the long-range-ordered phase. As is evident from Fig.20, the KT order of chirality is the sine or the partial disordered state. All these features are qualitatively the same as those observed in the $J' = J_1$ case. Hence, we conclude that the condition $J' = J_1$ is irrelevant, and the KT-type chiral transition identified in the $J' = J_1$ case would occur generically for other J' values so long as the nnn coupling J_2 is antiferromagnetic.

4.3   The case of ferromagnetic next-nearest-neighbor interaction: $J_2/J_1 = -0.5$

In this subsection, we consider the case in which the nnn interactions in the kagomé layers is *ferromagnetic*, fixing its magnitude to be $J_2 = -0.5J_1$. The antiferromagnetic inter-plane interaction J' is again set equal to J_1, *i.e.*, we assume $J' = J_1$ throughout this subsection.

In Fig.21, we show the temperature and size dependence of the specific heat per spin. The data show double peaks at $T/J_1 \simeq 0.52$ and at $T/J_1 \simeq 0.02$. In Fig.22, we show the temperature and size dependence of the linear and nonlinear susceptibilities per spin. Both the linear and nonlinear susceptibilities exhibit no appreciable anomaly in the investigated temperature range. This should be contrasted to the $J_2 > 0$ case where the linear susceptibility exhibits a clear cusp-like anomaly as shown in Fig.8(a).

In order to get information about the spin SRO, we show in Fig.23 the temperature and size dependence of the ferrimagnetic magnetizations associated with the $q = 0$ and the $\sqrt{3} \times \sqrt{3}$ modes, m_0 and $m_{\sqrt{3}}$, respectively. One can immediately see from these figures that, in contrast to the $J_2 > 0$ case shown in Fig.9, the $\sqrt{3} \times \sqrt{3}$ mode is stabilized over the $q = 0$ mode, reflecting the change in the sign of J_2. The higher specific-heat peak is well correlated with the onset of the $\sqrt{3} \times \sqrt{3}$ spin SRO.

The chirality-related quantities are shown in Figs.24 and 25. Fig.24 indicates that, as in other cases studied, the spins belonging to tetrahedron form locally non-coplanar structures, sustaining nontrivial chirality. Although $q_{\chi f}^{(2)}$ for a fixed size grows with decreasing temperature below $T/J_1 \simeq$ 0.1 as can be seen from Fig.25, probably reflecting the growth of $\bar{\chi}$ there, this tendency is more and more suppressed with increasing L. Furthermore, $q_{\chi f}^{(2)}$ values themselves remain small compared with those for $J_2 > 0$, and decreases rapidly with increasing L in contrast to the $J_2 > 0$ case. Hence, in the $J_2 < 0$ case, we conclude that there is no thermodynamic phase transition of the chirality, even though the specific heat has double peaks shown in Fig.21. The orgin of the lower specific-heat peak is not clear at the moment.

§5.   Discussion and Summary

We have studied by means of MC simulations the ordering properties of the antiferromagnetic Heisenberg model on a pyroclore slab. Due to the tetrahedron-based structure of this lattice, thermodynamic properties of the antiferromagnetic Heisenberg model on a pyroclore slab are quite different from those of the well-studied antiferromagnetic Heisenberg model on the kagomé lattice. In the case of the kagomé Heisenberg AF, the spin configuration selected at low temperatures is a coplanar one, while in the case of the pyroclore-slab AF, the spin configuration selected at low temperatures is a non-coplanar one sustaining the nontrivial chirality. We have performed a detailed numerical study of the chiral properties of the model. Among others, we have found that, when the nnn interaction on the kagomé layers is antiferromagnetic, the chiralities exhibit a KT-type phase transition at a finite temperature, with keeping the Heisenberg spins being paramagnetic. The KT ordered state of chirality is characterized by the sine-type $\sqrt{3} \times \sqrt{3}$ order (or the partial disorder). To the authors' knowledge, our present finding is the first case of *chiral* KT transition without accompanying any spin order.

Our present model is expected to capture some essential geometrical ingredients of SCGO, and indeed seems to account for some of the experimental features, *e.g.*, the occurrence of a finite-temperature transition above all, the cusp-like anomaly observed in the linear susceptibility,[11] or the existence of a specific-heat peak slightly above the transition temperature.[11] However, one immediately sees that some other experimental features remain unexplained. Experimentally, the negative divergence of the nonlinear susceptibility is observed at T_c,[11] which was not observed in our model.

One common property characterizing the SG-like freezing transition, including the one observed in SCGO, is the magnetic irreversibility, often detected as a notable difference between the field-cooled (FC) and zero-field-cooled (ZFC) dc susceptibilities.[11] In order to detect the possible difference between the FC and ZFC susceptibilities in the present model, we have also measured these quantities by MC simulation in the case of $J_2 = 0.5J_1$ and $J' = J_1$ where our model is found

to exhibit a chiral KT transition at $T = T_c \simeq 0.082J_1$. The system is gradually cooled or warmed in an applied field according to the standard heat-bath updating without the temperature-exchange process. Note that here the system is not necessarily equilibrated fully at each temperature. The result shown in Fig.26, however, reveals that there is no appreciable difference between the FC and ZFC susceptibilities even below $T_c \simeq 0.082J_1$. Therefore, our present model still fails to reproduce an important spin-glass feature observed in real SCGO.

Thus, while our present model might well capture some aspects of the ordering of SCGO so far neglected or unappreciated, it is still inadequate in fully describing the experimental result. Some important aspects which have not been taken into account in our present model, *e.g.*, the existence of quenched randomness, quantum fluctuations, or weak magnetic anisotropy *etc.*, might play an essential role in real SCGO. Further MC simulations taking account of some of these effects are now in progress.

The numerical calculation was performed on the Hitachi SR8000 at the supercomputer center, ISSP, University of Tokyo.

 1) *Magnetic Systems with Competing Interaction* ed. H.T. Diep, World Scientific (1994).
 2) M. Collins and O.A. Petrenko: Can. J. Phys. **75** (1997) 605.
 3) H. Kawamura: J. Phys. Condes. Matter **10** (1998) 4707.
 4) A. P. Ramirez: Ann. Rev. Mater. Sci. **24** (1994) 453.
 5) P. Schiffer and A. P. Ramirez: Comments Cond. Mat. Phys. **18** (1996) 21.
 6) M.J. Harris and M.P. Zinkin: Int. J. Mod. Phys. B **10** 417 (1996).
 7) J. T. Chalker, P. C. W. Holdsworth and E. F. Shender: Phys. Rev. Lett. **68** (1992) 855.
 8) J. N. Reimers: Phys. Rev. B **45** (1992) 7287.
 9) J. N. Reimers and A. J. Berlinsky: Phys. Rev. B **48** (1993) 9539.
10) R. Moessner and J.T. Chalker: Phys. Rev. Letters **80** (1998) 2929; Phys. Rev. B **58** (1998) 12049.
11) A. P. Ramirez, G. P. Espinosa and A. S. Cooper: Phys. Rev. Lett. **64** (1990) 2070; Phys. Rev. B **45** (1992) 2505.
12) C. Broholm, G. Aeppli, G. P. Espinosa and A. S. Cooper: Phys. Rev. Lett. **65** (1990) 3173.
13) S. -H. Lee, C.Broholm, G. Aeppli, T.G. Perring, B. Hessen and A. Taylor: Phys. Rev. Lett. **76** (1996) 4424.
14) H. Kawamura and S. Miyashita: J. Phys. Soc. Jpn. **53** (1985) 4138.
15) K. Hukushima and K. Nemoto: J. Phys. Soc. Jpn. **65** (1996) 1604.
16) K. Hukushima and H. Kawamura: Phys. Rev. E **61** (2000) R1008.
17) J. M. Kosterlitz and D. J. Thouless: J. Phys. C **6** (1973) 1181; *ibid.* C **7** (1974) 1046.
18) D. P. Landau: Phys. Rev. B **27** (1983) 5604.
19) H. Takayama, K. Matsumoto, H. Kawahara and K. Wada: J. Phys. Soc. Jpn. **52** (1983) 2888.
20) S. Fujiki, K. Shutoh, Y. Abe and S. Katsura: J. Phys. Soc. Jpn. **55** (1986) 3326.
21) S. Miyashita, H. Kitatani and Y. Kanada: J. Phys. Soc. Jpn. **60** (1991) 1523.
22) S. Alexander and P. Pincus: J. Phys. A **13** (1980) 263.
23) J. Jose, L. Kadanoff, S. Kirkpatrick and D. R. Nelson: Phys. Rev. B **16** (1977) 1217.
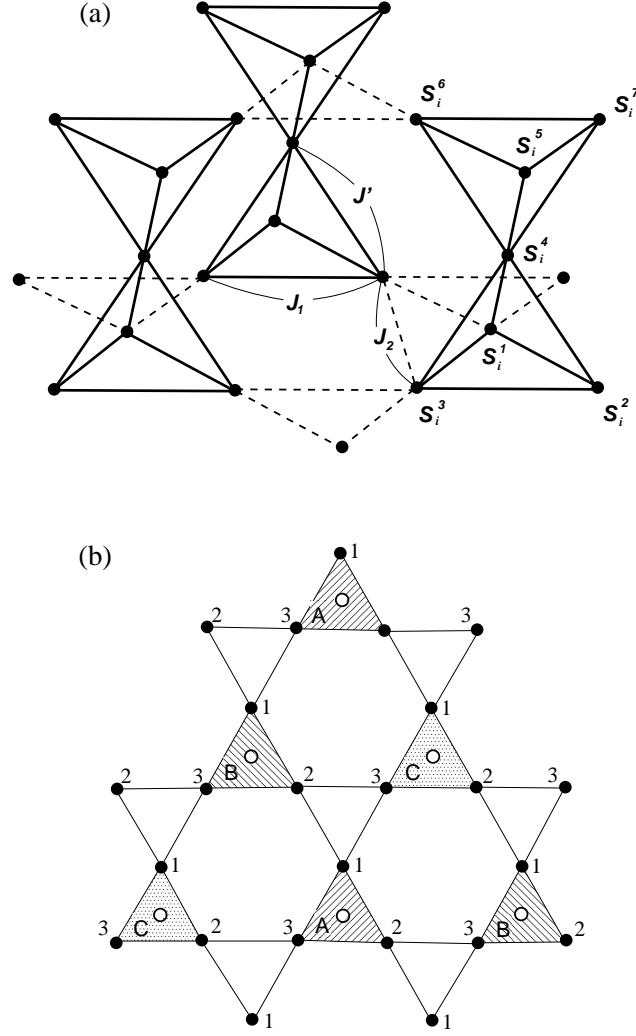
Figure 1: A pyrochlore-slab lattice: (a) The unit cell of the lattice consists of two corner-sharing tetrahedra illustrated by the solid lines. Each unit cell contains seven sites numbered from 1 to 7. Within the kagomé layers, there are the nearest-neighbor antiferromagnetic interaction J_1 and the next-nearest-neighbor interaction J_2, while, between the kagomé layers and the triangular layer sandwiched by the two kagomé layers, there is the antiferromagnetic interaction J' along the edge of tetrahedron: (b) The lower kagomé layer consisting of the sites 1, 2 and 3, denoted by the solid circle. The open circle denotes the apical site of tetrahedron (site 4). The upward triangle corresponds to the bottom plane of tetrahedron, which form the triangular lattice. These upward triangles are grouped into three types denoted by A, B and C, each forming the three inter-penetrating triangular sublattices.

1
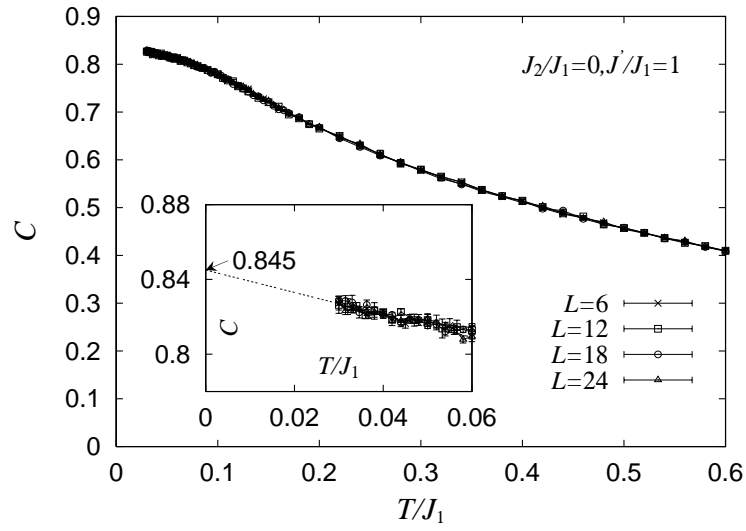
Figure 2: The temperature and size dependence of the specific heat per spin for the case $J_2/J_1 = 0$ and $J'/J_1 = 1$. The inset is a magnified view of the low-temperature regime.
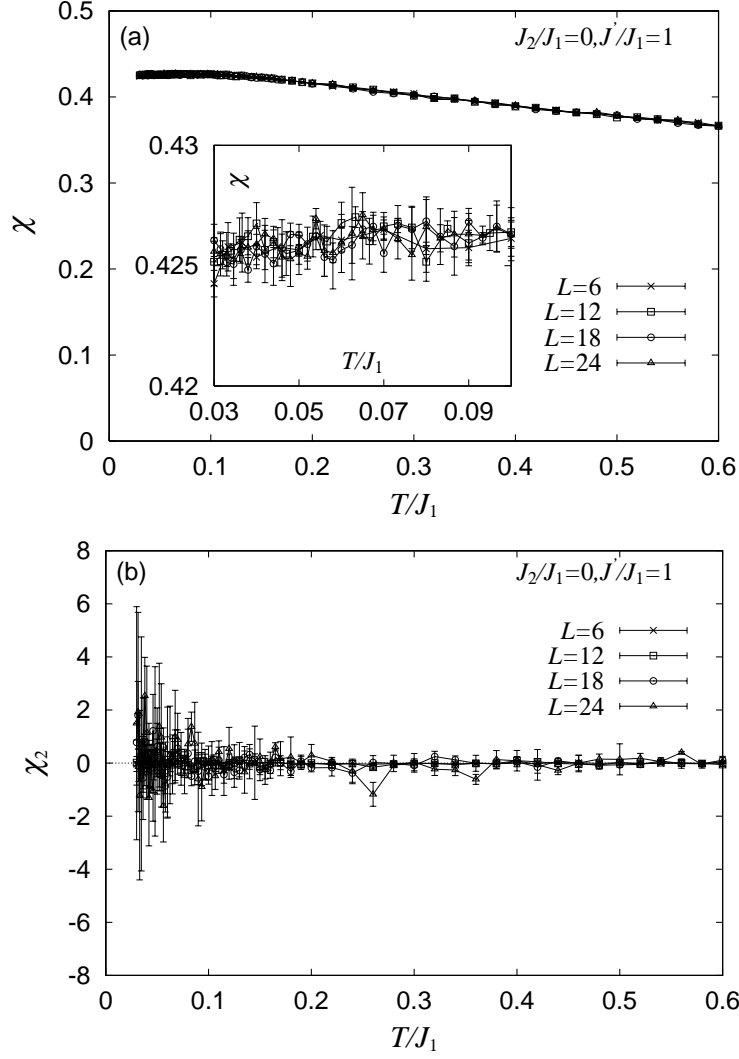
Figure 3: The temperature and size dependence of (a) the linear susceptibility per spin, and (b) the nonlinear susceptibility per spin, for the case $J_2/J_1 = 0$ and $J'/J_1 = 1$. The inset is a magnified view of the low-temperature regime.
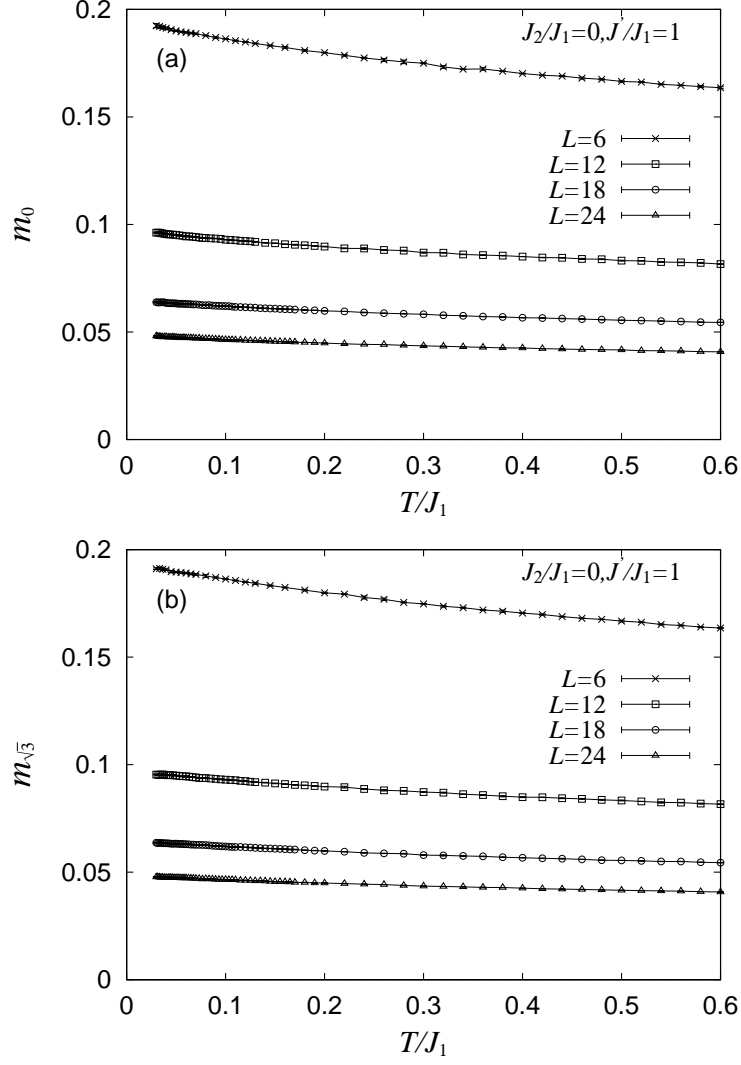
Figure 4: The temperature and size dependence of the ferrimagnetic magnetization per spin associated with (a) the $q = 0$ mode, and (b) the $\sqrt{3} \times \sqrt{3}$ mode, for the case $J_2/J_1 = 0$ and $J'/J_1 = 1$.
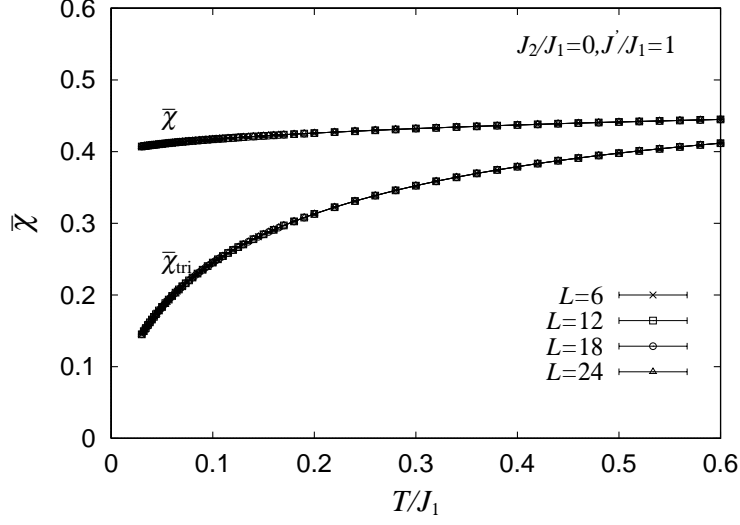
Figure 5: The temperature and size dependence of the mean local amplitude of the chirality for the case $J_2/J_1 = 0$ and $J'/J_1 = 1$. $\bar{\chi}$ and $\bar{\chi}_{\text{tri}}$ represent the local chirality defined at the upward and downward triangles on the kagomé layer, respectively.
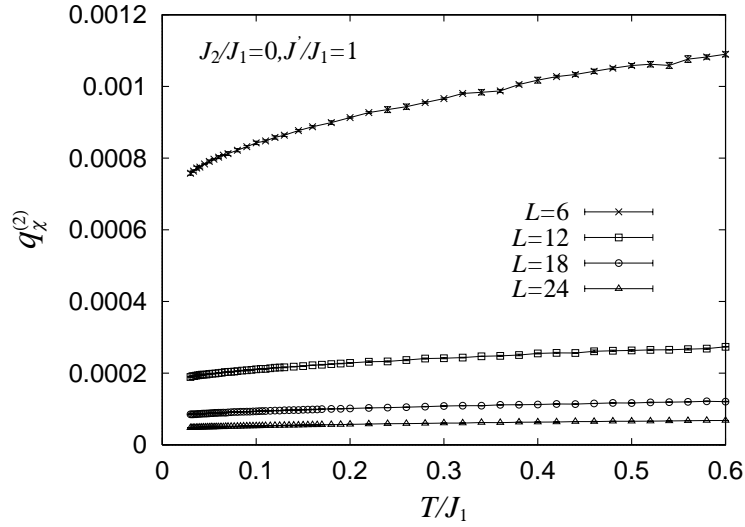
Figure 6: The temperature and size dependence of the chiral-glass order parameter for the case $J_2/J_1 = 0$ and $J'/J_1 = 1$.

5
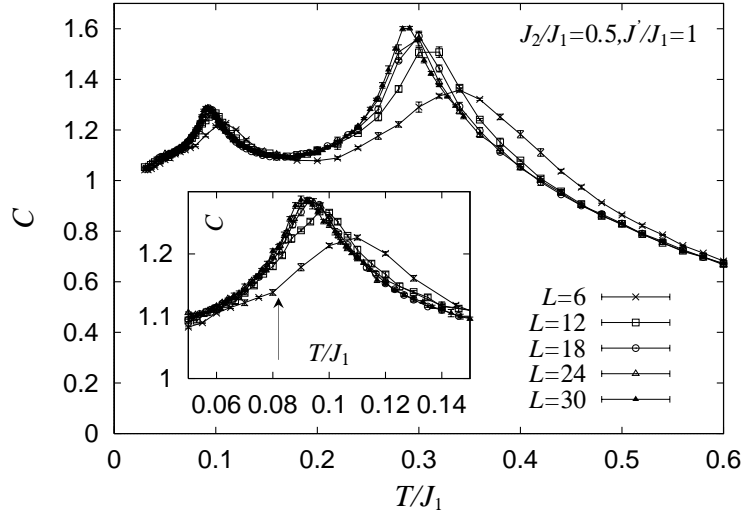
Figure 7: The temperature and size dependence of the specific heat per spin for the case $J_2/J_1 = 0.5$ and $J'/J_1 = 1$. The inset is a magnified view of the low-temperature regime. The arrow indicates the transition point.
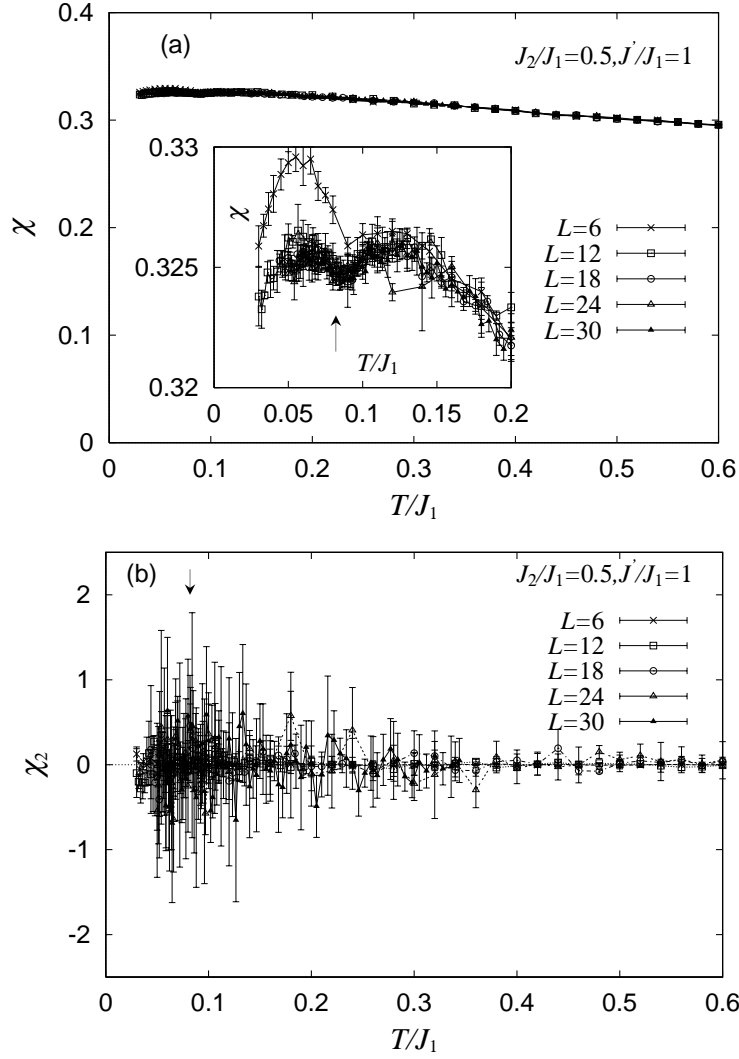
Figure 8: The temperature and size dependence of the (a) linear susceptibility per spin, and (b) the nonlinear susceptibility per spin, for the case $J_2/J_1 = 0.5$ and $J'/J_1 = 1$. The inset is a magnified view of the low-temperature regime. The arrow indicates the transition point.
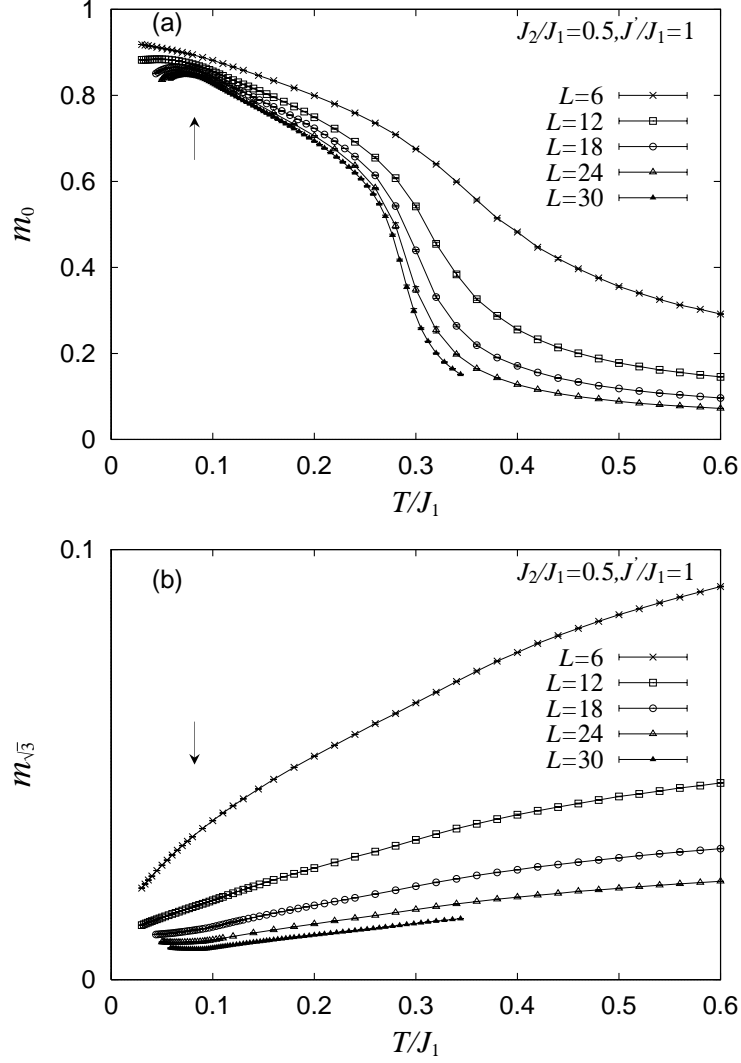
Figure 9: The temperature and size dependence of the ferrimagnetic magneti-zation per spin associated with (a) the $q = 0$ mode, and (b) the $\sqrt{3} \times \sqrt{3}$ mode, for the case $J_2/J_1 = 0.5$ and $J'/J_1 = 1$. The arrow indicates the transition point.
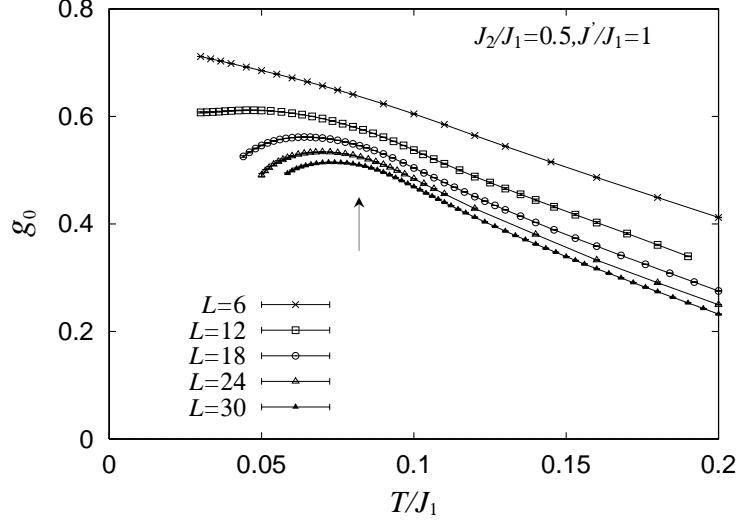
Figure 10: The temperature and size dependence of the spin Binder ratio associated with the $q = 0$ mode for the case $J_2/J_1 = 0.5$ and $J'/J_1 = 1$. The arrow indicates the transition point.
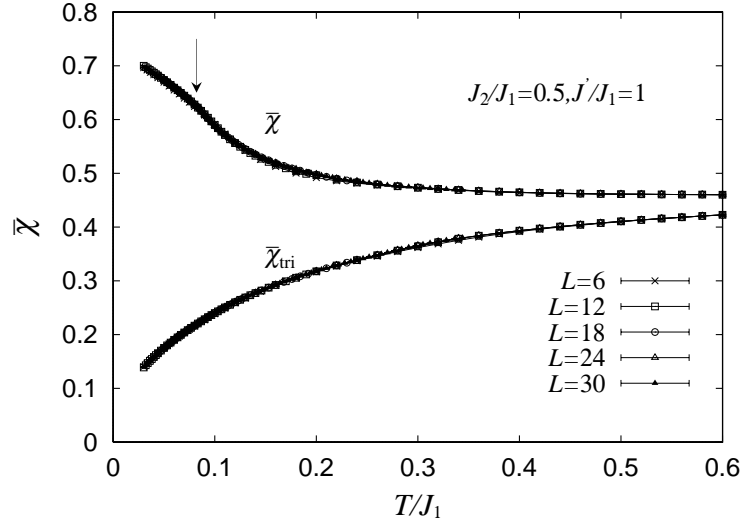
Figure 11: The temperature and size dependence of the mean local amplitude of the chirality for the case $J_2/J_1 = 0.5$ and $J'/J_1 = 1$. $\bar{\chi}$ and $\bar{\chi}_{\rm tri}$ represent the local chirality defined at the upward and downward triangles on the lower kagomé layer. The arrow indicates the transition point.

9
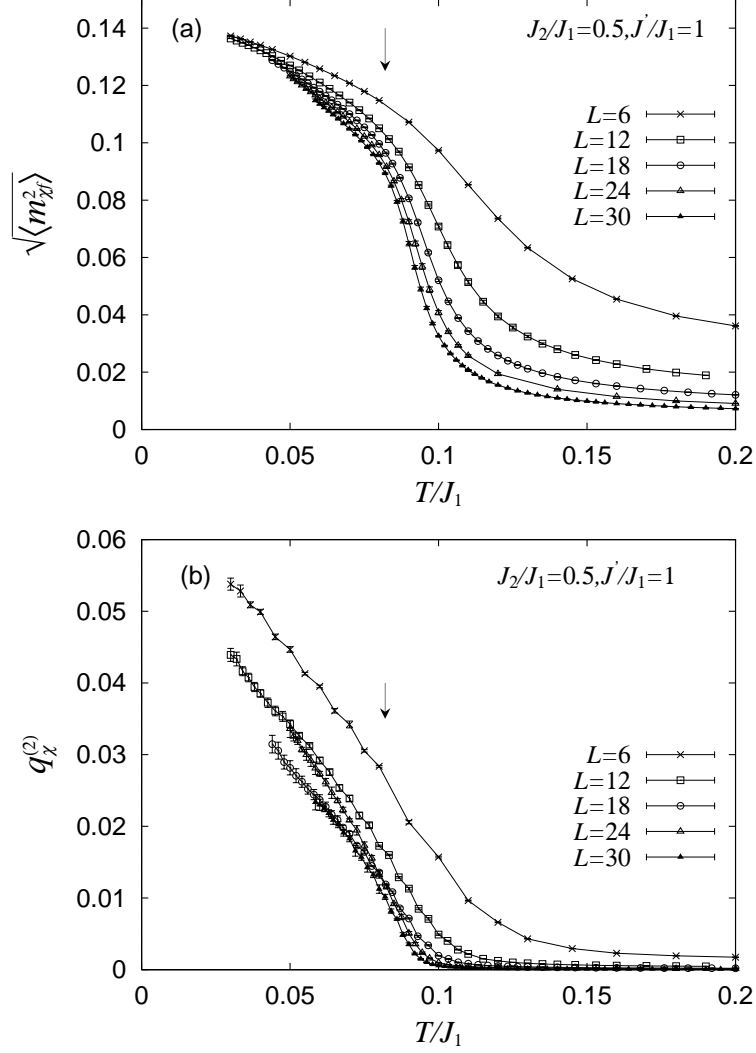
Figure 12: The temperature and size dependence of (a) the ferrimagnetic (staggered) chirality, and (b) the chiral-glass order parameter, for the case $J_2/J_1 = 0.5$ and $J'/J_1 = 1$. The arrow indicates the transition point.
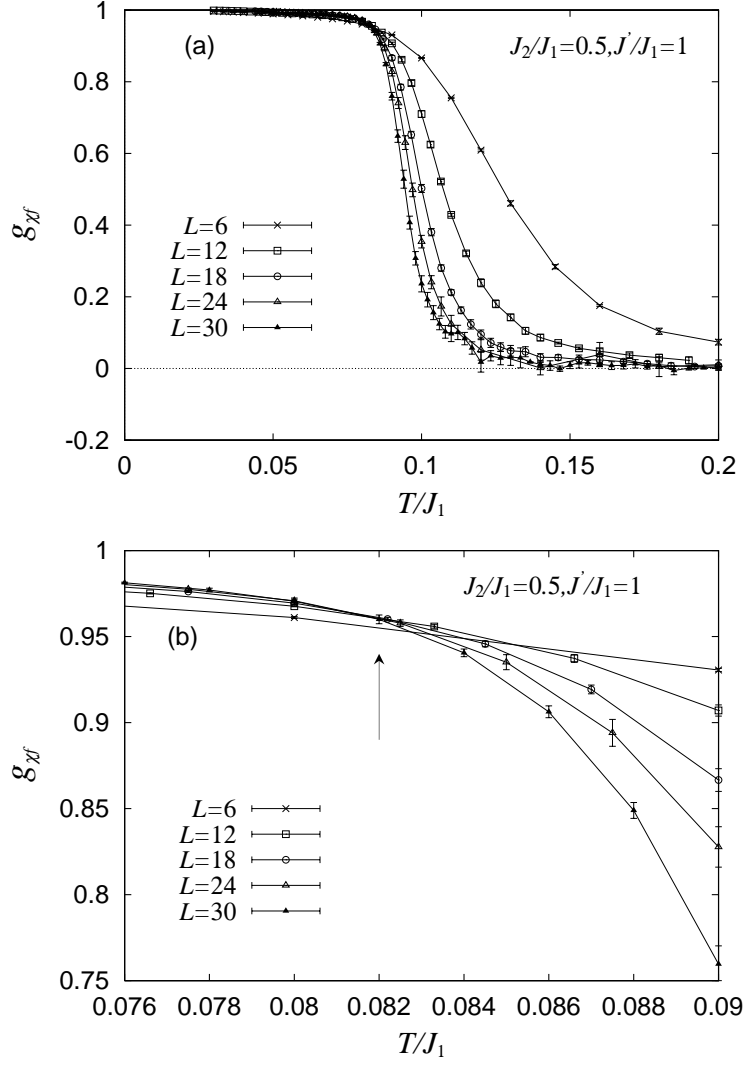
Figure 13: (a) The temperature and size dependence of the chiral Binder ratio for the case $J_2/J_1 = 0.5$ and $J'/J_1 = 1$. (b) A magnified view of the transition region. The arrow indicates the transition point.
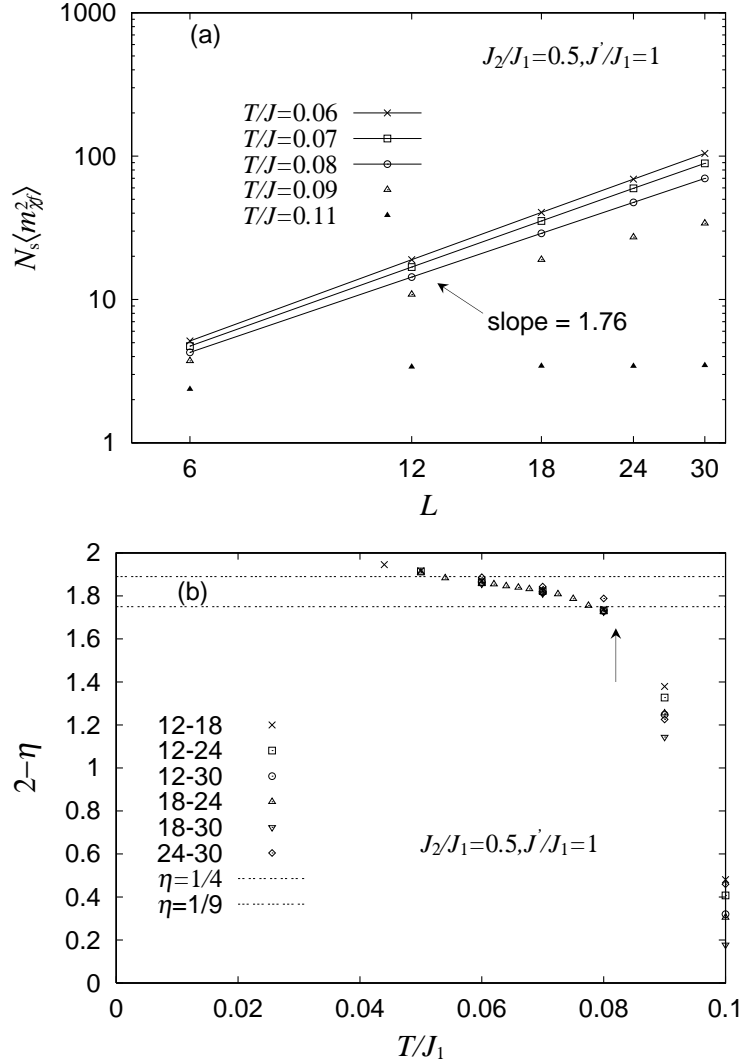
Figure 14: (a) Log-log plot of the ferrimagnetic (staggered) chiral susceptibility versus the system size L at several temperatures, for the case $J_2/J_1 = 0.5$ and $J'/J_1 = 1$. (b) The slope of the data in (a), which should be equal to $2 - \eta$, is plotted versus the temperature. Two numbers in the legend represent the L and L' values used in the fit: See text for details. The broken horizontal lines represent the lines corresponding to $\eta = 1/4$ and $\eta = 1/9$.
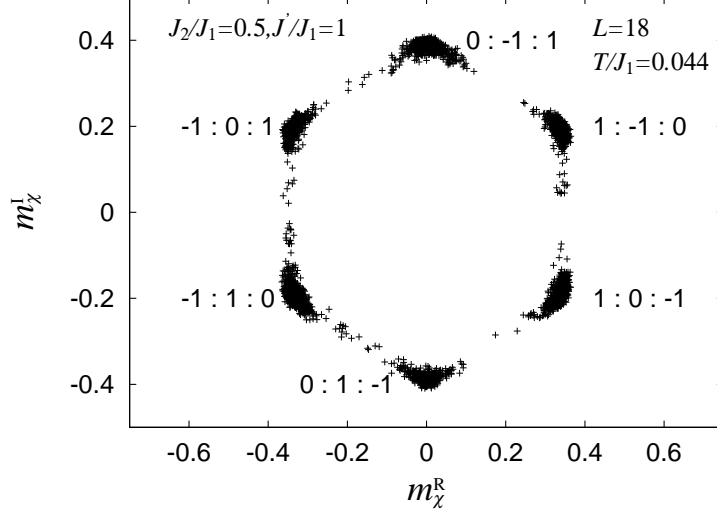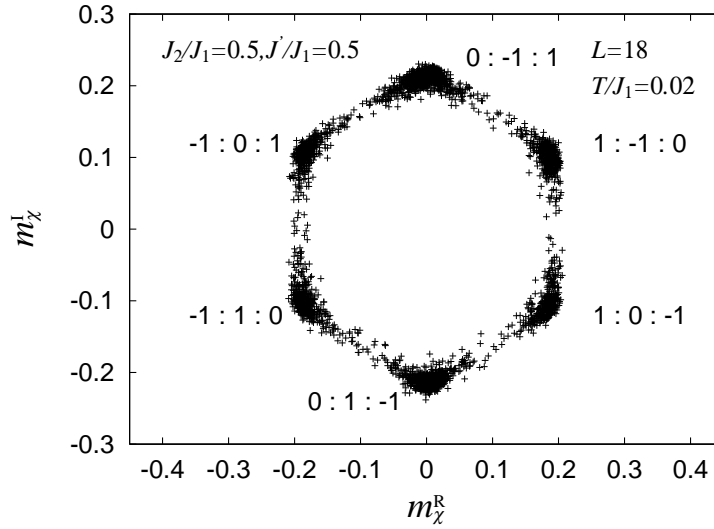
Figure 15: Distribution of (m_χ^R, m_χ^I), defined by eqs. (14) and (15), for the case $J_2/J_1 = 0.5$ and $J'/J_1 = 1$. The temperature is $T/J_1 = 0.044$, well below the transition point $T_c/J_1 \simeq 0.082$. The lattice size is $L = 18$.
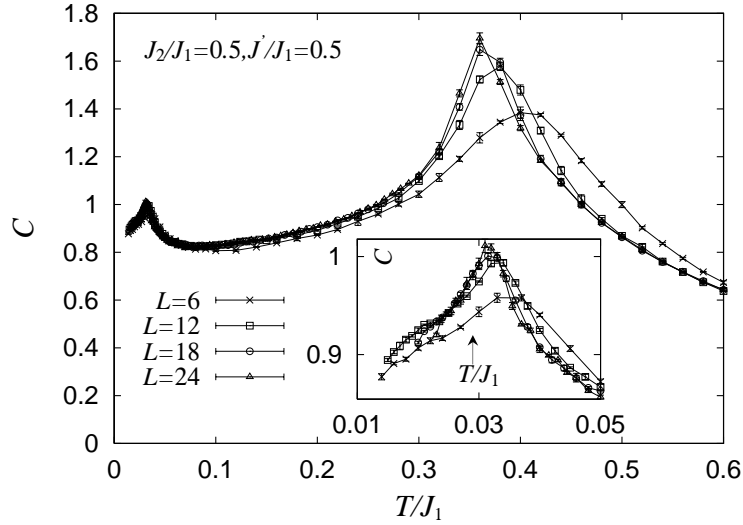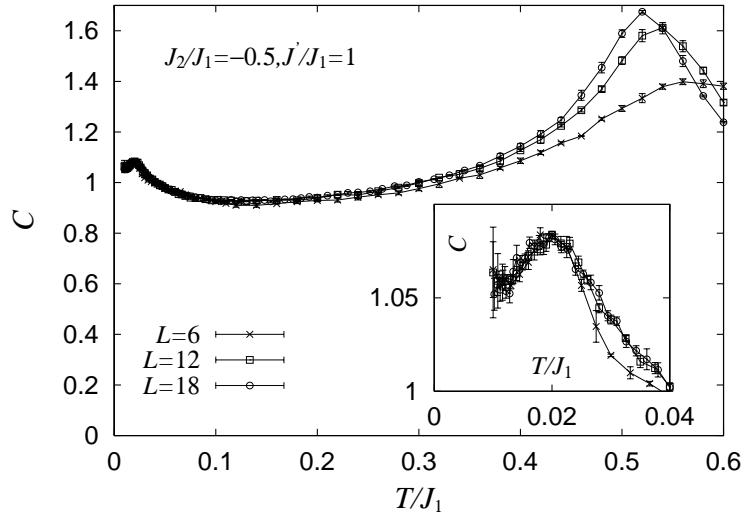

Figure 16: The temperature and size dependence of the specific heat per spin for the case $J_2/J_1 = 0.5$ and $J'/J_1 = 0.5$. The inset is a magnified view of the low-temperature regime. The arrow indicates the transition point.

13
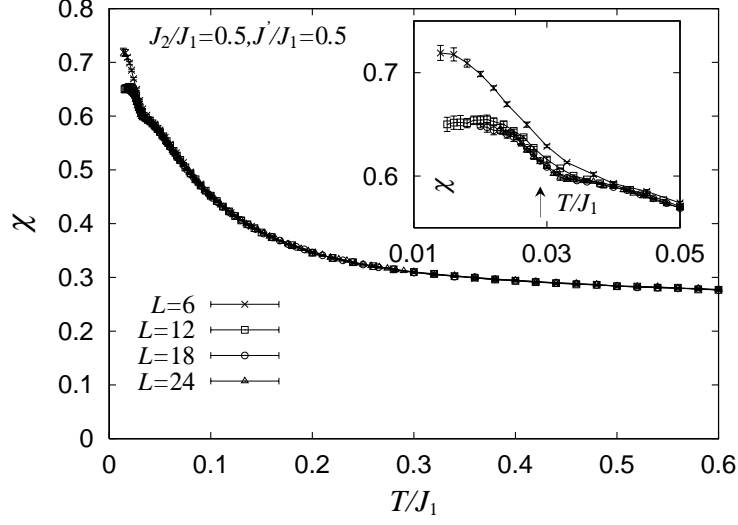
Figure 17: The temperature and size dependence of the linear susceptibility per spin for the case $J_2/J_1 = 0.5$ and $J'/J_1 = 0.5$. The inset is a magnified view of the low-temperature regime. The arrow indicates the transition point.
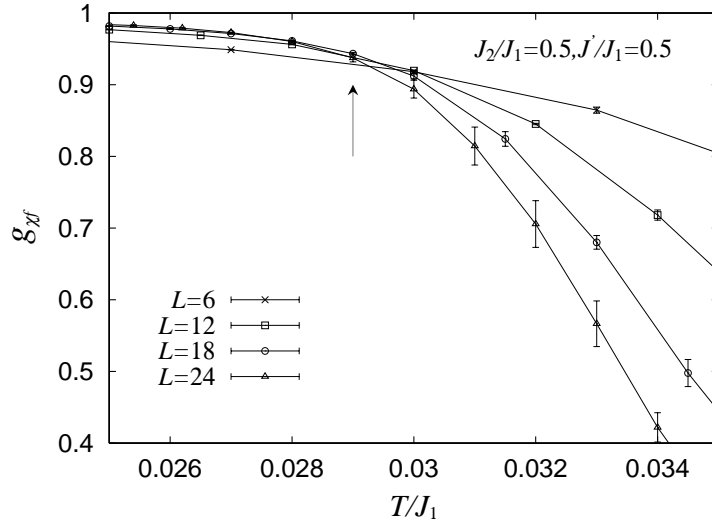
Figure 18: The temperature and size dependence of the chiral Binder ratio for the case $J_2/J_1 = 0.5$ and $J'/J_1 = 0.5$ in the transition region. The arrow indicates the transition point.

14
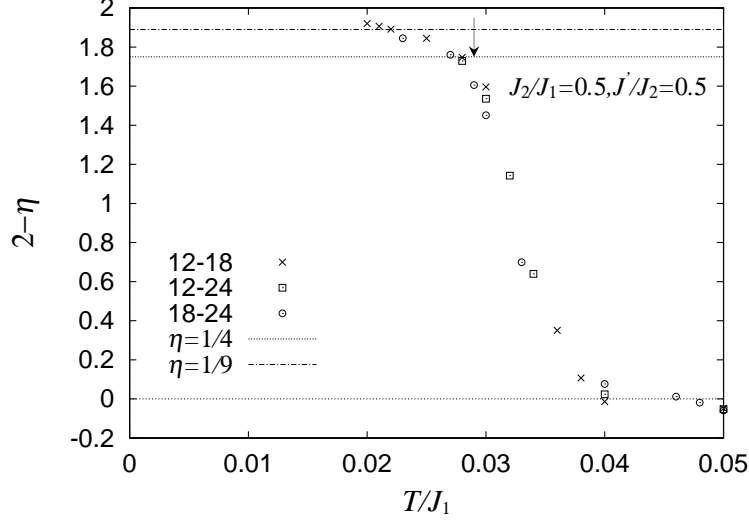
Figure 19: The estimated exponent $2 - \eta$ is plotted versus the temperature for the case $J_2/J_1 = 0.5$ and $J'/J_1 = 0.5$. The two numbers in the legend represent the L and L' values used in the fit: See text for details. The dashed horizontal lines represent the lines corresponding to $\eta = 1/4$ and $\eta = 1/9$.

Figure 20: Distribution of (m_χ^R, m_χ^I), defined by eqs. (14) and (15), for the case $J_2/J_1 = 0.5$ and $J'/J_1 = 0.5$. The temperature is $T/J_1 = 0.02$, well below the transition point $T_c/J_1 \simeq 0.029$. The lattice size is $L = 18$.

15

Figure 21: The temperature and size dependence of the specific heat per spin for the case $J_2/J_1 = -0.5$ and $J'/J_1 = 1$. The inset is a magnified view of the low-temperature regime.
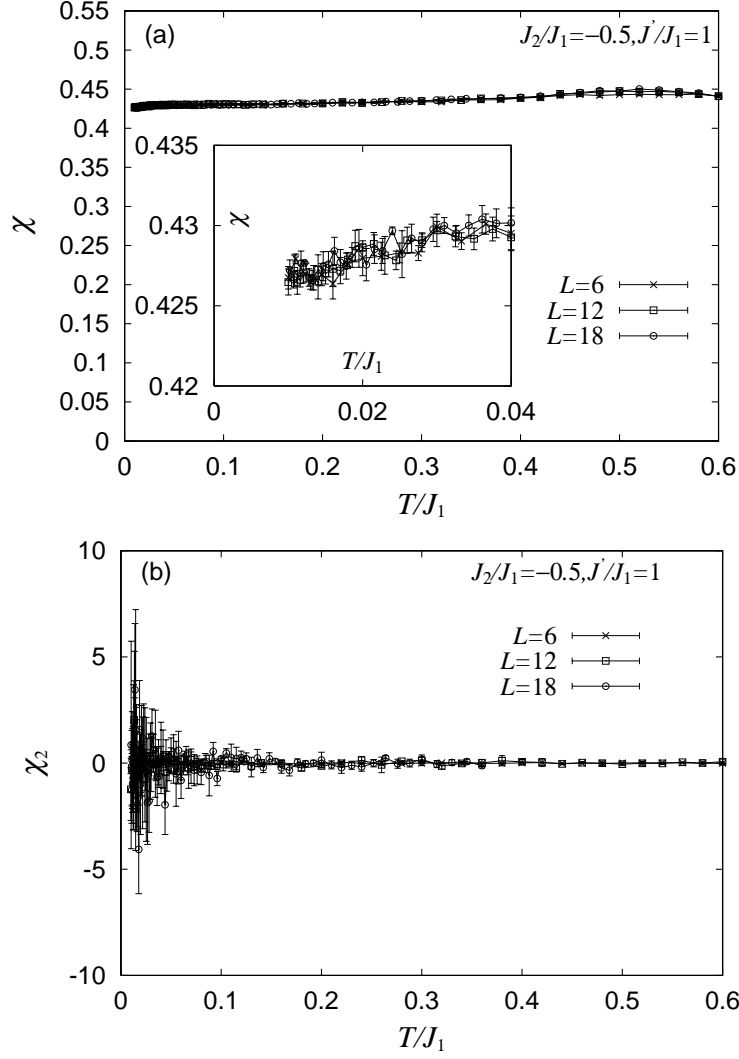
Figure 22: The temperature and size dependence of (a) the linear susceptibility per spin, and (b) the nonlinear susceptibility per spin, for the case $J_2/J_1 = -0.5$ and $J'/J_1 = 1$. The inset is a magnified view of the low-temperature regime.
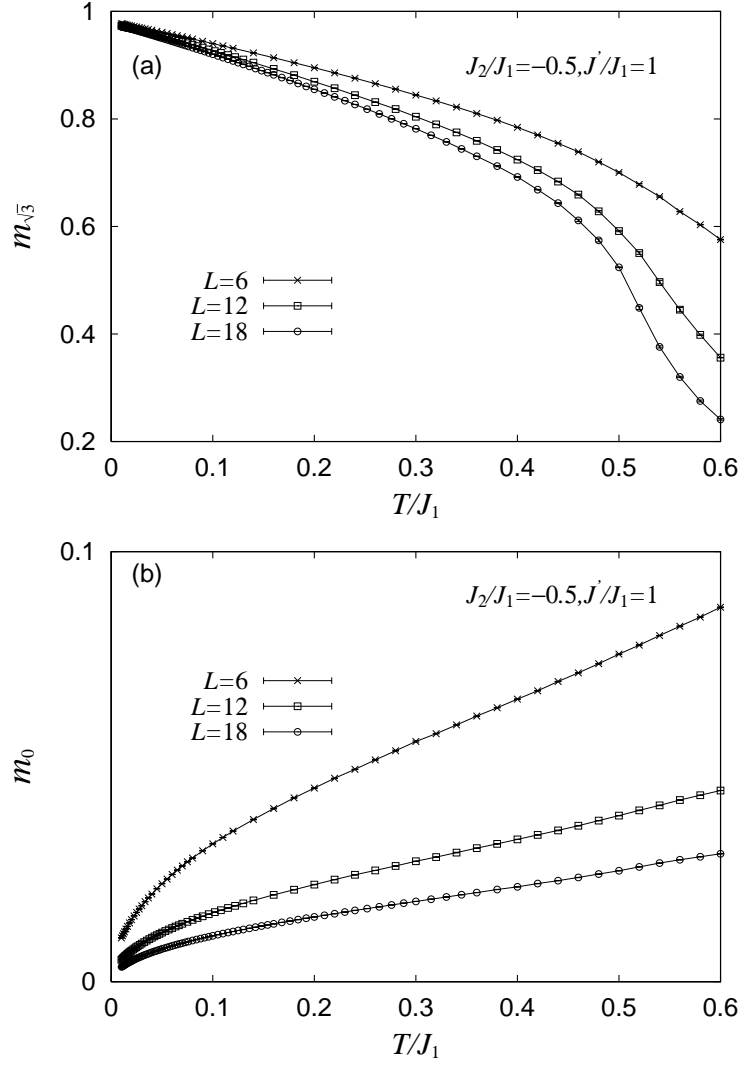
Figure 23: The temperature and size dependence of the ferrimagnetic magnetization per spin associated with the (a)$\sqrt{3} \times \sqrt{3}$ mode, and (b) the $q = 0$ mode, for the case $J_2/J_1 = -0.5$ and $J'/J_1 = 1$.
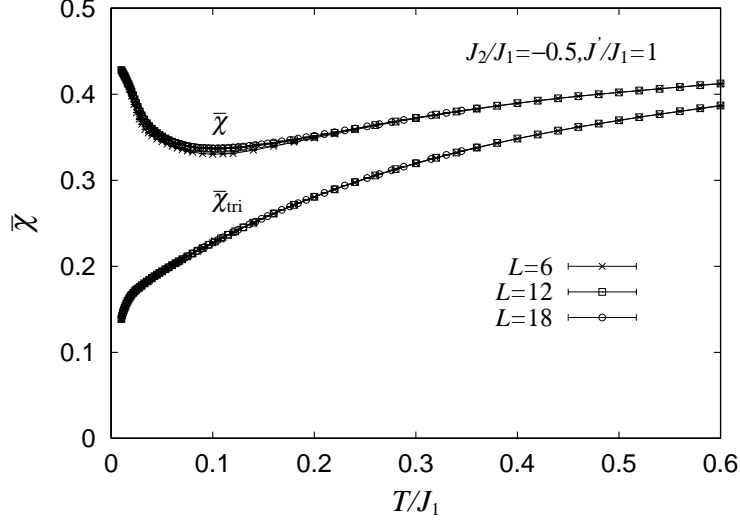
Figure 24: The temperature and size dependence of the mean local amplitude of the chirality for the case $J_2/J_1 = -0.5$ and $J'/J_1 = 1$. $\bar{\chi}$ and $\bar{\chi}_{\text{tri}}$ represent the local chirality defined at the upward and downward triangles on the lower kagomé layer.
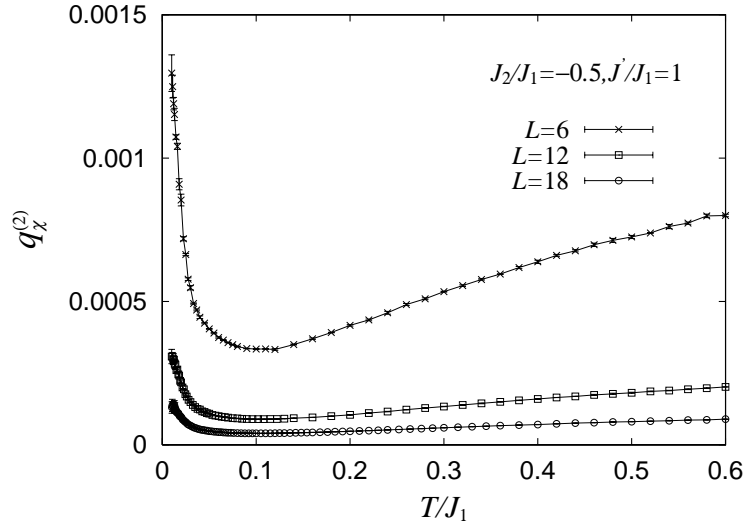

Figure 25: The temperature and size dependence of the chiral-glass order parameter for the case $J_2/J_1 = -0.5$ and $J'/J_1 = 1$.
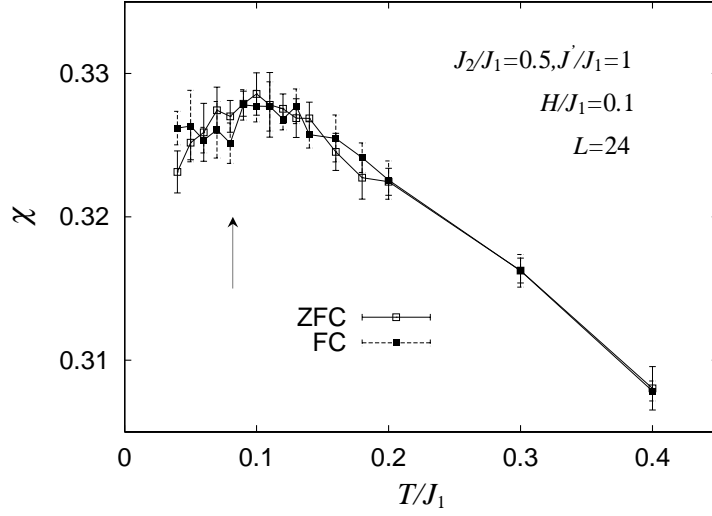
Figure 26: The temperature dependence of the field-cooled (FC) and zero-field-cooled (ZFC) susceptibilities for the case $J_2/J_1 = 0.5$ and $J'/J_1 = 1$. The intensity of the applied field is $H/J_1 = 0.1$, and the lattice size is $L = 24$. At each temperature, total of 10^6 MCS are generated, of which the latter 5×10^5 MCS are used to measure the magnetization. FC magnetization is measured by gradually cooling the system in a field in steps from $T/J_1 = 0.4$ to $T/J_1 = 0.04$ across the transition temperature $T_c/J_1 \simeq 0.082$. ZFC magnetization is measured, first by quenching the system from infinite temperature to $T/J_1 = 0.04$, and then by gradually warming the system in a field in steps from $T/J_1 = 0.04$ to $T/J_1 = 0.4$ across the transition temperature.